Influence of microstructural evolution on tensile properties of friction stir welded joint of rolled SiCp/AA2009-T351 sheet

D.R. Ni [a], D.L. Chen [b], D. Wang [a], B.L. Xiao [a], Z.Y. Ma [a,*]

[a] Shenyang National Laboratory for Materials Science, Institute of Metal Research, Chinese Academy of Sciences, 72 Wenhua Road, Shenyang 110016, China
[b] Department of Mechanical and Industrial Engineering, Ryerson University, 350 Victoria Street, Toronto, Ontario, Canada M5B 2K3

A B S T R A C T

To elucidate the intrinsic factors which decreased the strength and ductility of friction stir welded (FSW) joints of precipitation-strengthened aluminium matrix composites, 3 mm thick rolled 17 vol.% SiCp/AA2009 composite sheet in T351 condition was subjected to FSW and detailed microstructure examinations. The microstructure of the base metal was characterized by high dislocation density and few precipitates. After FSW, low dislocation density and a few coarse θ (Al_2Cu) precipitates were detected in the nugget zone, whereas a great number of coarse θ and S (Al_2CuMg) precipitates and greatly decreased dislocation density were observed in the heat-affected zone (HAZ). Therefore, the HAZ showed the lowest hardness throughout the whole joint and became the weakest region, where fracture occurred during tensile testing. The FSW joint exhibited a good combination of strength and ductility with the ultimate tensile strength, elongation and joint efficiency reaching 443 MPa, 4.7% and 77%, respectively.

© 2013 Elsevier Ltd. All rights reserved.

1. Introduction

Metal–matrix composites (MMCs) are attractive materials for automotive, aerospace, and many other applications due to their superior mechanical and physical properties [1–3]. Among them, particle-reinforced aluminium matrix composites (AMCs) have developed considerably as a result of their low cost, isotropic properties, and desirable deformability [4,5].

In order to enable the wide utilization of AMCs, effective joining methods such as solid state and fusion processes become of practical importance. However, it is difficult to achieve defect-free welds by using conventional fusion welding techniques due to the presence of the ceramic particles. Problems such as the incomplete mixing of the parent and filler materials, the presence of porosity, and the formation of excess eutectic and deleterious phases are difficult to avoid in the fusion welded joints [6,7]. For example, Storjohann et al. [6] reported that fusion welding could not produce sound AMC welds due to the decomposition of particles or the serious reaction of particles with molten Al matrix. In this case, solid-state welding techniques are highly desirable to achieve potentially good AMC joints.

As a solid-state joining technique, friction stir welding (FSW) is rapidly developing and has proved to be successful and effective in welding aluminium alloys [8,9]. It is considered a promising welding method of joining AMCs, because the drawbacks of fusion

welding can be avoided in FSW. In the past few years, the FSW of AMCs was attempted and the microstructures and mechanical properties of the FSW joints were studied, including Al_2O_3p/AA7005 [10,11], Al_2O_3p/AA6061 [11–15], SiCp/AA2009 [16–19], B_4Cp/AA6063 [20], TiB_2p/Al [21], Mg_2Sip/Al–9.7Mg–5.5Si [22], and TiCp/Al [23]. FSW has been shown to result in a more homogeneous distribution of the particles and their breakup and bluntness due to the effect of severe plastic deformation and material mixing; furthermore, the grain sizes of the matrices were greatly refined due to recrystallization.

Root et al. [15] reported that in the nugget zone (NZ) of FSW Al_2O_3p/AA6061 there existed a crystallographic texture gradient which showed similar trends to that of an unreinforced Al alloy. Feng et al. [17] pointed out that the NZ of FSW SiCp/AA2009 was characterized by fine and equiaxed recrystallized grains with dominant high angle grain boundaries, and the texture in the NZ was significantly weakened. Compared to fusion welded joints, the FSW AMC joints exhibited good tensile properties due to the improved microstructures. In some cases, the NZ of FSW AMC joints even showed better tensile strengths than the base metal (BM) [18,24]. Furthermore, the FSW AMC joints also showed good fatigue resistance, fracture toughness, and fatigue crack propagation resistance [25–27].

However, severe wear of the steel tool was widely reported during FSW of AMCs due to the presence of hard ceramic particles, and the wear tended to increase with increasing rotation rate and welding speed [28–30]. The wear not only reduced the lifetime of the tool, but also affected the properties of the weld due to

---

* Corresponding author. Tel./fax: +86 24 83978908.
  E-mail address: zyma@imr.ac.cn (Z.Y. Ma).

the existence of wear debris. The formation of a Cu_2FeAl_7 phase was identified at or near SiC particle interfaces in the NZ of the FSW SiCp/AA2009 joints under both as-FSW and T4 conditions [18,31]. The formation of Cu_2FeAl_7 might lower the interfacial bonding between SiC and Al matrix and reduce the number of precipitates due to the dilution of the Cu element. Furthermore, Uzun [32] reported that in a FSW SiCp/AA2124 the NZ contained porosities/cracks around/in some coarse particles. Undoubtedly, these defects are undesirable for the FSW joints.

Although several studies on the FSW of AMCs were reported, most of them were focused on as-cast and as-extruded composites with a thickness of more than 4 mm, and information on FSW of as-rolled composite sheets is lacking. Moreover, previous studies [10–13,18,20] showed that FSW apparently decreased the strength and ductility of the precipitation-strengthened AMCs due to the softening in the heat-affected zone (HAZ); however, the intrinsic factor resulting from the microstructure evolution has not been illuminated clearly.

In this study, 3 mm thick 17 vol.% SiCp/AA2009 rolled sheet was subjected to FSW and the microstructures of the FSW joint were carefully examined with the aim of elucidating the relationship between the local microstructure evolution and tensile properties of the joint. A wear-resisting cermet tool was used to eliminate the negative effect of tool wear on the microstructure and properties of FSW AMC joints.

2. Materials and methods

17 vol.% SiCp reinforced AA2009 matrix composite produced by a powder metallurgy technique was used in this study. The nominal chemical composition of the AA2009 alloy was 4.26Cu–1.61Mg–0.01Si–0.009Fe (wt.%). SiC particles (SiCp) with an average particle size of 7 μm were adopted as reinforcement. The hot pressed ingot was first extruded and subsequently rolled into 3 mm thick sheet with the rolling direction perpendicular to the extrusion direction. The rolled sheet was T351-treated (solutionised at 502 °C for 1 h, water quenched, cold rolled with 15% reduction and then aged at room temperature for more than one month) and then subjected to FSW perpendicular to the rolling direction using a gantry FSW machine at a tool rotational rate of 1000 rpm and a welding speed of 50 mm min^{-1}. A cermet tool with a concave shoulder 14 mm in diameter and a cylindrical pin 5 mm in diameter and 2.7 mm in length with a triangular tip was used.

After FSW, the welded sheets were kept at room temperature for one month to age naturally. The specimens for microstructural examination were cross-sectioned perpendicular to the FSW direction. The microstructures were examined using scanning electron microscopy (SEM, Quanta 600) and transmission electron microscopy (TEM, FEI TECNAIG20). The specimens for SEM were prepared by mechanical grinding, polishing, and etching using Keller's reagent. Thin foils for TEM were cut from the BM, HAZ, and NZ, respectively, and thinned by ion milling. Phase identification was conducted via X-ray diffractometry (XRD) (D/max 2500 PC) with Cu Kα radiation. Differential scanning calorimetry (DSC) (Q1000V9.4 Build 287) analysis was conducted on specimens in the form of $\phi 4 \times 2$ mm. The specimens were heated from 25 to 550 °C at a heating rate of 5 °C min^{-1} under a flowing argon atmosphere with a pure alumina crucible.

Vickers hardness and tensile tests were conducted in accordance with ASTM: E384-11e1 (Standard Test Method for Knoop and Vickers Hardness of Materials) and ASTM: E8/E8M-11 (Standard Test Methods for Tension Testing of Metallic Materials), respectively. The hardness profiles were produced along the mid-thickness of the sheet at an interval of 0.5 mm on the cross-section of the weld by using a computerized Buehler hardness tester under a load of 1000 g for 15 s. Tensile specimens with a parallel section of $32 \times 5.6 \times 3$ mm were electrical discharge machined perpendicular to the FSW direction, and ground with SiC papers up to grit #600 to achieve a smooth surface. Tensile tests were conducted at a constant strain rate of 1×10^{-3} s^{-1} at room temperature, and at least two specimens were tested for each group. After the tensile tests, the fracture surfaces were examined using SEM. The failed joints were mounted, polished, and etched to determine the fracture location.

3. Results

3.1. Microstructure characteristics

Welds of about 1200 mm long were achieved by using the cermet tool. No wear was visible on the tool, indicating that the tool is suitable for welding AMCs. Fig. 1 shows a typical cross-sectional macrograph of the FSW joint. No defects were detected in the joint, showing that a sound join was achieved. The FSW joint included four zones: the NZ, the thermomechanically-affected zone (TMAZ), the HAZ, and the BM. The NZ exhibited basically a basin shape. No onion rings, which are the typical feature observed in the NZ of FSW aluminium alloys, were detected in the NZ of the present FSW composite.

Fig. 2 shows the SEM microstructures of the FSW joint. In the BM, SiC particles showed a polygonal morphology and were homogeneously distributed in the matrix with the long axis parallel to the rolling direction (Fig. 2a). After FSW, the SiCp were more homogeneously distributed in the NZ. Meanwhile, the size and aspect ratio of the SiCp were visibly decreased, and the edges and corners of the SiCp in the NZ, especially in the centre and bottom of the NZ, were obviously blunted (Fig. 2b–d) compared to the sharp SiC particles in the BM.

Fig. 3 shows the DSC curves of the BM, NZ, and HAZ, respectively. The DSC curves revealed that complex reactions appeared in the three samples in the heating process. These reactions could be primarily divided into five parts: Region A at 50–100 °C and Region C at 200–300 °C for exothermic reactions; Region B at 100–200 °C, Region D at 300–500 °C, and Region E beyond 505 °C for endothermic reactions. Region C contained two distinctly overlapped reactions for both the BM (peaks 1 and 2) and the NZ (peaks 1′ and 2′), but it contained only one reaction for the HAZ (peak 3). Both the intervals between peaks 1 and 2 and between peaks 1′ and 2′ are about 35 °C. Compared to peaks 1 and 2, peaks 1′ and 2′ became weaker and shifted to temperatures that were higher by about 20 °C.

Fig. 4 shows the XRD patterns of the BM, NZ, and HAZ, respectively. For all the samples, in addition to Al and SiC peaks, weak Al_2CuMg and Mg_2Si peaks were detected in the XRD patterns. The Al_2CuMg peaks should result from some large Al_2CuMg particles which were difficult to dissolve during the solution treatment and FSW processes. On the other hand, Mg_2Si are common impurities in the AMCs. Unlike in the BM, Al_2Cu peaks appeared in the NZ and HAZ of the FSW sample.

Fig. 5 shows the TEM microstructures of the BM, NZ, and HAZ, respectively. Almost no precipitates were detected in the BM, but a high density of dislocations was clearly observed (Fig. 5a). The diffraction patterns further confirmed that no precipitates existed

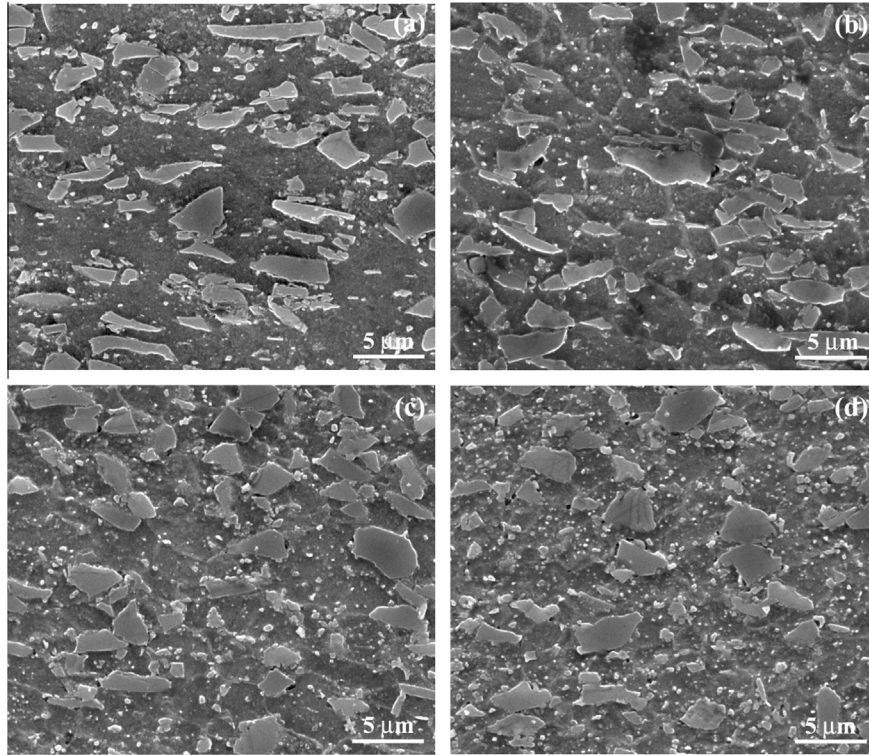**Fig. 1.** Cross-sectional macrostructure of FSW SiCp/AA2009 joint.

Fig. 2. SEM microstructures of FSW SiCp/AA2009 joint: (a) BM, (b) top of NZ, (c) centre of NZ, and (d) bottom of NZ.
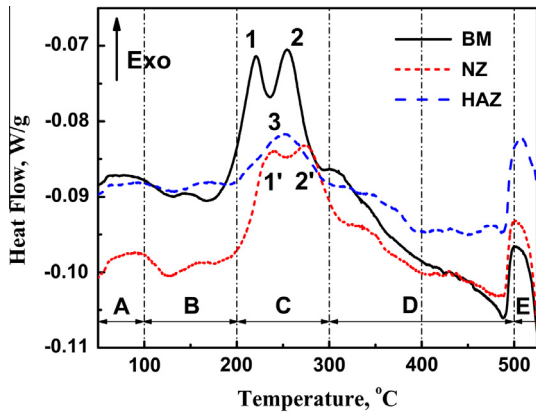

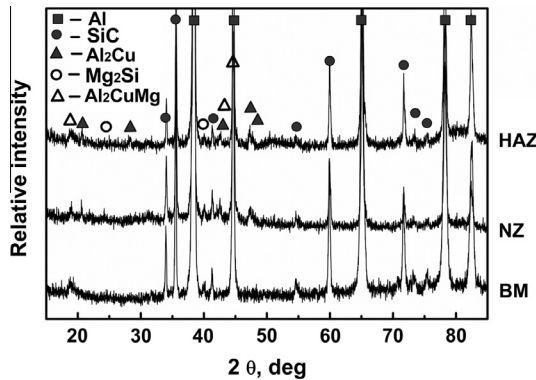**Fig. 3.** DSC curves of FSW SiCp/AA2009 joint in various zones.

Fig. 4. XRD patterns of FSW SiCp/AA2009 joint in various zones.

in the BM (Fig. 5d). However, a few coarse precipitates and a lower density of dislocations were observed in the NZ (Fig. 5b). Compared to the BM and the NZ, many coarse precipitates were distributed in the HAZ (Fig. 5c). These precipitates could be divided into two kinds according to their morphologies and sizes: fine needle-shaped precipitates and coarse granular precipitates. According to the selected area diffraction patterns (Fig. 5e and f) and other researchers' studies [18,33,34], the fine needle-shaped precipitates should be S phase (Al_2CuMg), whereas the coarse granular precipitates should be θ phase (Al_2Cu). It is also seen that few dislocations were present in the HAZ.

3.2. Microhardness and tensile properties

Fig. 6 shows a typical hardness profile along the mid-thickness of the FSW joint. It can be seen that the hardness distribution exhibits a typical "W" shape, with the lowest hardness located in the HAZ. The hardness of the BM and the NZ is about 200 HV and 160 HV, respectively. The lowest hardness of the HAZ (~130 HV) on the retreating side (RS) is slightly lower than that (~135 HV) on the advancing side (AS), with a distance about 6 mm from the weld centerline for the former and about 7.5 mm for the latter. Beyond the hardness troughs, the hardness increased gradually with increasing the distance from the weld centerline and reached the level of the BM at a distance of about 15 mm. Compared to the BM, the hardness of the SZ and the HAZ decreased about 20% and 35%, respectively.

Fig. 7 shows typical engineering stress versus engineering strain curves for the BM and the FSW joint. The yield strength (YS), ultimate tensile strength (UTS) and elongation are 508 MPa, 581 MPa and 4.3% for the BM, and 274 MPa, 443 MPa and 4.7% for the FSW joint, respectively. The FSW joint showed lower strengths than the BM with a joint efficiency of about 77%, but the joint showed a similar ductility to that of the BM.
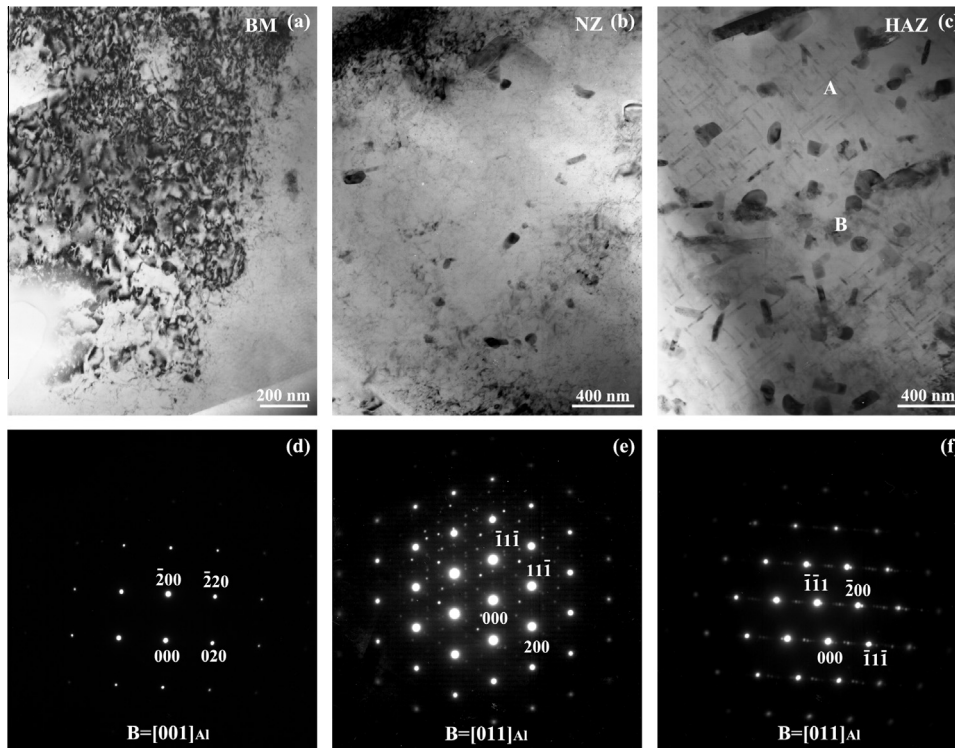
Fig. 5. TEM images of FSW SiCp/AA2009 joint: (a), (b), and (c) bright field images of BM, NZ, and HAZ, respectively; (d) diffraction pattern corresponding to (a) showing no precipitates; (e and f) selected area diffraction patterns corresponding to point A and point B in (c) showing formation of S and θ, respectively.
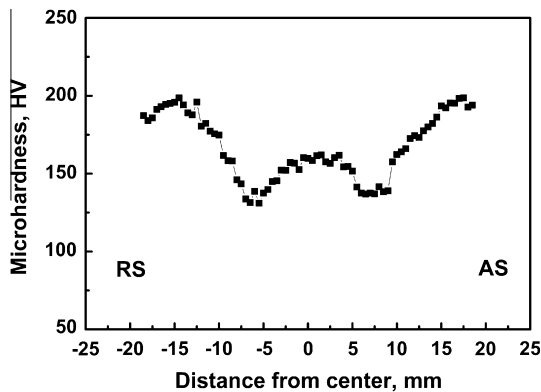

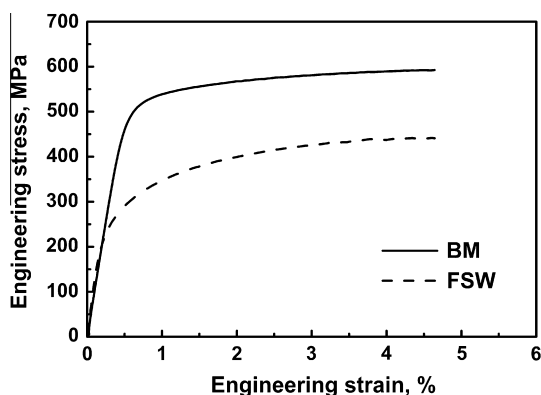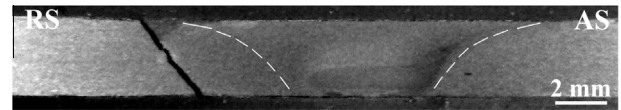**Fig. 6.** A typical microhardness profile of FSW SiCp/AA2009 joint.

Fig. 8. Optical micrograph showing failure location of FSW SiCp/AA2009 joint.

The fracture of the FSW joint occurred in the HAZ on the RS (Fig. 8). The fracture surface of the BM (Fig. 9a) was characterized by some large and shallow Al dimples and cracked SiCp, and micro-cracks were also observed. Compared to the BM, the joint showed a quite different fracture surface (Fig. 9b). The fracture surface was smoother, with many fine A1 dimples being observed. Furthermore, a very small amount of pull-out marks of SiCp were detected, whereas few broken SiC particles and cracks were visible.

4. Discussion

4.1. Microstructural characteristics

Tool wear presents a great challenge for FSW of AMCs. Feng et al. [18,31] reported that Cu_2FeAl_7 phase was formed in the NZ of FSW SiCp/AA2009 due to the wear of the steel tool. In this study, a cermet tool was selected and it showed no visible wear after welding for a long distance. This is beneficial to elucidating the real microstructural changes in the joint.

Ma et al. [19] reported that the shape of the NZ was greatly affected by the tool rotation rate in 8 mm thick FSW SiCp/AA2009 joints. At low rotation rates of 400 and 600 rpm the NZ showed basically a cylindrical shape. However, when the tool rotation rate was increased to 1000 rpm, the NZ consisted of two parts: a basin shape in the upper region and an elliptical shape in the lower region. They considered that the change in the NZ shapes could be associated with two factors. First, a higher tool rotation rate
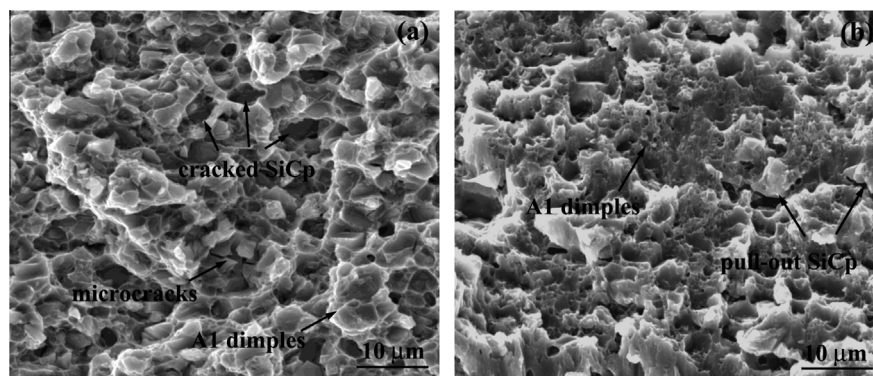

Fig. 7. Typical engineering stress versus engineering strain curves of BM and FSW SiCp/AA2009 joint.

Fig. 9. Typical SEM images showing tensile fracture surfaces: (a) BM, and (b) FSW SiCp/AA2009 joint.

tends to generate an elliptical NZ. Second, the severe wear of tool threads during FSW changed the flow characteristics of the material. In the present study, the NZ showed a basin shape at a rotation rate of 1000 rpm (Fig. 1), which is quite different from that reported by Ma et al. [19].

It is noted that no onion rings were visible in the NZ, and this is different from the FSW AMC joints with a larger thickness: 8 mm thick SiCp/AA2009 at 600 rpm [18,19] and 6 mm thick SiCp/AA2124 at 800 rpm [32], in which distinct onion rings appeared. These results showed that in addition to the rotation rate, the thickness of AMC joints greatly affects the NZ shape and the onion-ring microstructures. The possible reason is that the sheet in the present study is too thin, so the influence of the shoulder on the material flow becomes more significant than that of the pin.

After FSW, some large SiCp were fragmented in the NZ and the distribution of SiCp became more homogeneous due to the intense deformation and mixing (Fig. 2). Meanwhile, the rotating pin also knocked off the corners and sharp edges of the large SiCp, and therefore blunted the sharp SiCp. Similar microstructure changes during FSW were also reported in an as-extruded SiCp/AA2009 [18]. Due to dynamic recrystallization (DRX), the grains in the NZ showed an equiaxed morphology and their sizes were smaller than those in the BM.

4.2. Precipitates evolution

The precipitation sequences in the Al–Cu–Mg alloys are extremely complex and can be divided into two kinds depending on the Cu/Mg ratio, and S and θ are two equilibrium phases in the alloys [33–36]. Both the precipitation sequences could take place simultaneously or separately as follows: SSS (supersaturated solid solution) $\rightarrow$ GPB (Guinier–Preston–Bagaryatsky) zone $\rightarrow$ S″/GPB2 $\rightarrow$ S′ $\rightarrow$ S (Al$_2$CuMg) or SSS $\rightarrow$ GP zones $\rightarrow$ θ″ $\rightarrow$ θ′ $\rightarrow$ θ (Al$_2$Cu).

Recently, Wang and Starink [37] conducted the DSC investigations on the as-solutionized Al–4.2Cu–1.5Mg–0.6Mn alloys with 0.5 Si and 0.08 Si, respectively. Two distinct exothermic peaks were observed in the temperature range of 250–350 °C, which corresponded to two types of S phases, Type I and Type II. Type II S phase is a noncoherent precipitate and is more stable than Type I. They suggested that the sequence for the formation of S phase by homogeneous nucleation is SSS $\rightarrow$ Clusters $\rightarrow$ S″/GPB2 $\rightarrow$ S (Type I) $\rightarrow$ S (Type II).

Similar to the traditional terminology for the precipitates, one could term Type I S and Type II S as S′ and S, respectively. The formation of Type II S phase was strongly dependent on solution treatment and cold working. For example, in the solution-treated, quenched, and subsequently cold-worked samples, extensive formation of Type I S phase occurred, whereas the formation of Type

II S phase was suppressed. Furthermore, Type I S phase shifted to a lower temperature with increasing deformation. This was attributed to an increase in heterogeneous nucleation sites for the S phase, predominantly at dislocations [37].

However, the SiCp reinforced Al–Cu–Mg composites may show different precipitation sequences from their matrix alloys. For example, Rodrigo et al. [38] observed two overlapped exothermic peaks at 250–300 °C in the DSC curve of a SiCp/AA2009. They considered that the first peak corresponded to the formation of S′ phase, whereas the second was due to the formation of θ′ phase. Recently, Jin et al. [39] also reported that the overlapped exothermic peaks correspond to the precipitation of S′ and θ′ phases, and considered that the S′ precipitation would be accelerated due to the increased dislocation density.

The DSC results of the present study are similar to those of Wang and Starink [37]. Five main effects can be generally identified from the DSC patterns (Fig. 3). In Region A, the exothermic peak is due to the growth of Cu–Mg co-clusters. In Region B, the endothermic effect may be attributed to the dissolution of Cu–Mg co-clusters. In Region C, generally the exothermic effect is due to the formation of Al$_2$CuMg and Al$_2$Cu precipitates: peaks 1 and 1′ should be attributed to the precipitation of S′, and peaks 2 and 2′ should be attributed to the precipitation of S and θ′, whereas peak 3 should be attributed to the precipitation of θ′ phase due to the lack of magnesium. In Region D, the broad endothermic effect is due to the progressive dissolution of the S and θ′ precipitates. In Region E, the sharp endothermic peak is due to the melting of S and θ eutectics.

In the naturally aged Al–Cu–Mg alloys, the dominant strengthening phases are GPB zones which are considered to be a short-range ordering of Cu and Mg solute atoms and which have cylindrical shapes with sizes of about several nanometers, and they are difficult to detect even by TEM [34]. Generally, it can be deduced from the DSC curves that all the samples contained GPB zones, but the content of GPB zones decreased from the BM to the HAZ. The Al$_2$Cu peaks were detected in the XRD patterns of the NZ and the HAZ (Fig. 4), showing the existence of θ phase. The TEM results further confirmed that no visible precipitates were observed in the BM, but a few coarse θ existed in the NZ and many fine needle-shaped S and coarse granular θ existed in the HAZ (Fig. 5). As a result, it can be concluded from the comprehensive results of DSC, XRD, and TEM that the main strengthening phases are the GPB zones, GPB zones + θ, and S + θ, respectively, in the BM, NZ, and HAZ.

FSW can be considered as a complicated hot-working process and it firstly dissolves the precipitates into the Al matrix. During cooling these dissolved precipitates re-precipitated out in the NZ and some of the re-precipitated precipitates transformed into θ due to the slow cooling rate in air. Many S and θ phases were found

in the HAZ, and this was due to the coarsening of the precipitates during the FSW thermal cycle.

The TEM examinations also showed that the microstructure of the BM was characterized by a high density of dislocations (Fig. 5a), which were produced due to the large coefficient of thermal expansion mismatch strain between the Al matrix and SiCp. The dislocations in the NZ were generated during the air cooling after FSW (Fig. 5b), and the dislocation density was lower than that in the BM because of the occurrence of the DRX and the slow cooling rate in air. The dislocations were greatly decreased in the HAZ (Fig. 5c), and this was attributed to the dislocation release resulting from the FSW thermal cycle.

Peaks 1′ and 2′ in the NZ are much weaker than their counterparts in the BM, and this can be attributed to their different initial microstructures. As discussed above, a large number of GPB zones existed in the BM at room temperature, thus more precipitates precipitated out during the DSC test. In the NZ, the number of GPB zones is fewer than that in the BM, so fewer precipitates precipitated out during DSC heating. However, in the HAZ, only a few GPB zones remained, therefore only peak 3 appeared during the DSC test.

The shifting to higher temperatures of peaks 1′ and 2′ in the NZ can be ascribed to the low dislocation density in the NZ, which led to a decrease in heterogeneous nucleation sites for precipitates. However, it is noted that the FSW process did not change the interval between peaks 1′ and 2′. Considering different dislocation densities in the two regions, these results suggest that the dislocation density greatly influenced the precipitating behaviour.

4.3. Microhardness and tensile properties

As shown in Fig. 6, the hardness distribution of the FSW SiCp/AA2009-T351 joint exhibited a typical "W" shape. Similar-shaped hardness profiles were also observed in the FSW joints of heat-treatable 2xxx Al alloys [40–42]. However, the FSW composite joint in this study showed obviously higher hardness in all characteristic regions than the FSW 2xxx Al alloy joints, due to the existence of the SiCp. The hardness profile of FSW heat-treatable aluminium alloys greatly depends on the precipitate distribution and only slightly on the grain and dislocation structures. As shown in Figs. 3 and 5, for the BM under the T351 condition, the GPB zone greatly strengthened the Al matrix, therefore the BM exhibited the highest hardness of ∼200 HV. In the NZ, as discussed above, the GPB zones decreased whereas the θ increased, leading to a lower hardness of ∼160 HV. In the HAZ, the S and θ did not exert an obvious strengthening effect on the Al matrix, therefore the HAZ showed the lowest hardness of ∼130 HV. Thus, a typical "W" shaped hardness profile was observed for the FSW SiCp/AA2009-T351 joint. Feng et al. [18] measured the hardness profile of the FSW joint of an as-extruded SiCp/AA2009. They reported that the BM showed low hardness owing to the presence of coarse θ phase, whereas the NZ exhibited higher hardness due to the formation of fine θ″; however, after T4-treatment, similar hardness values were observed across the whole joint due to a similar precipitation-strengthening effect of θ″ in the various zones.

The tensile test results showed that the fracture occurred in the HAZ on the RS of the joint (Fig. 8). This is in agreement with the hardness profiles (Fig. 6). The FSW decreased the strengths of the BM without decreasing the ductility. The joint efficiency of FSW AMC joints was greatly affected by the initial and final conditions of the BMs and joints. For the soft as-cast composites, the FSW joint efficiency could reach nearly 100% with the fracture in the BM due to its lower strength [14,21,22]. For the precipitation-strengthened extruded composites, the strength and ductility of the FSW joint were apparently reduced due to the presence of HAZ softening, with the UTS, elongation and joint efficiency being lower than

330 MPa, 3.0% and 80%, respectively [10–13,18,20]. Compared to the previous results, the FSW joint in the present study exhibited better strength (443 MPa) and elongation (4.7%) with a considerably higher joint efficiency.

The Al dimples, microcracks, and cracked SiCp on the fracture surfaces of the BM (Fig. 9a) indicated that the BM failed in the form of both ductile failure of the matrix and fracture of SiCp. The joint showed quite different fracture surfaces compared to the BM, and it failed mainly by matrix ductile failure and partially by SiCp pull-out, resulting from the softening of the HAZ where the Al matrix had less constraint to the SiCp.

5. Conclusions

In summary, the following conclusions are reached:

(1) A sound FSW joint of 3 mm thick SiCp/AA2009-T351 sheet was achieved by using a cermet tool. No visible tool wear was observed.
(2) FSW resulted in the dissolution and re-precipitation of strengthening phases in the NZ and HAZ. The primary strengthening phases in the BM, NZ, and HAZ were GPB zones, GPB zones + θ, and S + θ, respectively. While the BM had a high density of dislocations, a low density of dislocations was observed in the NZ and HAZ.
(3) The FSW SiCp/AA2009-T351 joint exhibited a W-type hardness profile with the HAZ having the lowest hardness due to the coarsening of precipitates and the reduction of dislocation density. The YS, UTS, elongation, and joint efficiency of the FSW joint were 274 MPa, 443 MPa, 4.7%, and 77%, respectively, with the fracture occurring in the HAZ.

References

[1] Ibrahim IA, Mohamed FA, Lavernia EJ. Particulate reinforced metal matrix composites – a review. J Mater Sci 1991;26:1137–56.
[2] Lindroos VK, Talvitie MJ. Recent advances in metal matrix composites. J Mater Process Technol 1995;53:273–84.
[3] Tjong SC, Ma ZY. Microstructural and mechanical characteristics of in situ metal matrix composites. Mater Sci Eng R 2000;29:49–113.
[4] Jin P, Xiao BL, Wang QZ, Ma ZY, Liu Y, Li S. Effect of hot extrusion on interfacial microstructure and tensile properties of SiCp/2009Al composites fabricated at different hot pressing temperatures. J Mater Sci Technol 2011;27:518–24.
[5] Jin P, Xiao BL, Wang QZ, Ma ZY, Liu Y, Li S. Effect of hot pressing temperature on microstructure and mechanical properties of SiC particle reinforced aluminum matrix composites. Acta Metall Sinica 2011;47:298–304.
[6] Storjohann D, Barabash OM, Babu SS, David SA, Sklad PS, Bloom EE. Fusion and friction stir welding of aluminum–metal–matrix composites. Metall Mater Trans A 2005;36A:3237–47.
[7] Wang XH, Niu JT, Guan SK, Wang LJ, Cheng DF. Investigation on TIG welding of SiCp-reinforced aluminum–matrix composite using mixed shielding gas and Al–Si filler. Mater Sci Eng A 2009;499:106–10.
[8] Mishra RS, Ma ZY. Friction stir welding and processing. Mater Sci Eng R 2005;50:1–78.
[9] Nandan R, DebRoy T, Bhadeshia HKDH. Recent advances in friction-stir welding-process, weldment structure and properties. Prog Mater Sci 2008;53:980–1023.
[10] Ceschini L, Boromei I, Minak G, Morri A, Tarterini F. Effect of friction stir welding on microstructure, tensile and fatigue properties of the AA7005/10 vol.%Al₂O₃p composite. Compos Sci Technol 2007;67:605–15.

[11] Cavaliere P, Cerri E, Marzoli L, Dos Santos J. Friction stir welding of ceramic particle reinforced aluminium based metal matrix composites. Appl Compos Mater 2004;11:247–58.

[12] Marzoli LM, Strombeck AV, Dos Santos JF, Gambaro C, Volpone LM. Friction stir welding of an AA6061/Al$_2$O$_3$/20p reinforced alloy. Compos Sci Technol 2006;66:363–71.

[13] Ceschini L, Boromei I, Minak G, Morri A, Tarterini F. Microstructure, tensile and fatigue properties of AA6061/20 vol.%Al$_2$O$_{3p}$ friction stir welded joints. Composites Part A 2007;38:1200–10.

[14] Minak G, Ceschini L, Boromei I, Ponte M. Fatigue properties of friction stir welded particulate reinforced aluminium matrix composites. Int J Fatigue 2010;32:218–26.

[15] Root JM, Field DP, Nelson TW. Crystallographic texture in the friction-stir-welded metal matrix composite Al6061 with 10 vol pct Al$_2$O$_3$. Metall Mater Trans A 2009;40A:2109–14.

[16] Wang D, Xiao BL, Wang QZ, Ma ZY. Friction stir welding of SiCp/2009Al composite plate. Mater Des 2013;47:243–7.

[17] Feng AH, Xiao BL, Ma ZY. Grain boundary misorientation and texture development in friction stir welded SiCp/Al–Cu–Mg composite. Mater Sci Eng A 2008;497:515–8.

[18] Feng AH, Xiao BL, Ma ZY. Effect of microstructural evolution on mechanical properties of friction stir welded AA2009/SiCp composite. Compos Sci Technol 2008;68:2141–8.

[19] Ma ZY, Feng AH, Xiao BL, Fan JZ, Shi LK. Microstructural evolution and performance of friction stir welded aluminum matrix composites reinforced by SiC particles. Mater Sci Forum 2007;539–543:3814–9.

[20] Chen XG, da Silva M, Gougeon P, St-Georges L. Microstructure and mechanical properties of friction stir welded AA6063–B$_4$C metal matrix composites. Mater Sci Eng A 2009;518:174–84.

[21] Vijay SJ, Murugan N. Influence of tool pin profile on the metallurgical and mechanical properties of friction stir welded Al–10 wt.% TiB$_2$ metal matrix composite. Mater Des 2010;31:3585–9.

[22] Nami H, Adgi H, Sharifitabar M, Shamabadi H. Microstructure and mechanical properties of friction stir welded Al/Mg$_2$Si metal matrix cast composite. Mater Des 2011;32:976–83.

[23] Gopalakrishnan S, Murugan N. Prediction of tensile strength of friction stir welded aluminium matrix TiCp particulate reinforced composite. Mater Des 2011;32:462–7.

[24] Amirizad M, Kokabi AH, Abbasi Gharacheh M, Sarrafi R, Shalchi B, Azizieh M. Evaluation of microstructure and mechanical properties in friction stir welded A356+15%SiCp cast composite. Mater Lett 2006;60:565–8.

[25] Cavaliere P, Rossi GL, Di Sante R, Moretti M. Thermoelasticity for the evaluation of fatigue behavior of 7005/Al$_2$O$_3$/10p metal matrix composite sheets joined by FSW. Int J Fatigue 2008;30:198–206.

[26] Pirondi A, Collini L. Analysis of crack propagation resistance of Al–Al$_2$O$_3$ particulate-reinforced composite friction stir welded butt joints. Int J Fatigue 2009;31:111–21.

[27] Pirondi A, Collini L, Fersini D. Fracture and fatigue crack growth behaviour of PMMC friction stir welded butt joints. Eng Fract Mech 2008;75:4333–42.

[28] Prado RA, Murr LE, Shindo DJ, Sota KF. Tool wear in the friction-stir welding of aluminum alloy 6061+20% Al$_2$O$_3$: a preliminary study. Scripta Mater 2001;45:75–80.

[29] Shindo DJ, Rivera AR, Murr LE. Shape optimization for tool wear in the friction-stir welding of cast Al359–20% SiC MMC. J Mater Sci 2002;37:4999–5005.

[30] Fernandez GJ, Murr LE. Characterization of tool wear and weld optimization in the friction-stir welding of cast aluminum 359 + 20% SiC metal–matrix composite. Mater Charact 2004;52:65–75.

[31] Feng AH, Ma ZY. Formation of Cu$_2$FeAl$_7$ phase in friction-stir-welded SiCp/Al–Cu–Mg composite. Scripta Mater 2007;57:1113–6.

[32] Uzun H. Friction stir welding of SiC particulate reinforced AA2124 aluminium alloy matrix composite. Mater Des 2007;28:1440–6.

[33] Rodrigo P, Poza P, Utrilla MV, Ureña A. Identification of σ and Ω phases in AA2009/SiC composites. J Alloys Compd 2009;482:187–95.

[34] Gouma PI, Lloyd DJ, Mills MJ. Precipitation processes in Al–Mg–Cu alloys. Mater Sci Eng A 2001;319–321:439–42.

[35] Ratchev P, Verlinden B, De Smet P, Van Houtte P. Precipitation hardening of an Al–4.2 wt% Mg–0.6 wt% Cu alloy. Acta Mater 1998;46:3523–33.

[36] Wang SC, Starink MJ. Precipitates and intermetallic phases in precipitation hardening Al–Cu–Mg–(Li) based alloys. Int Mater R 2005;50:193–215.

[37] Wang SC, Starink MJ. Two types of S phase precipitates in Al–Cu–Mg alloys. Acta Mater 2007;55:933–41.

[38] Rodrigo P, Poza P, Utrilla V, Ureña A. Effect of reinforcement geometry on precipitation kinetics of powder metallurgy AA2009/SiC composites. J Alloys Compd 2009;479:451–6.

[39] Jin P, Xiao BL, Wang QZ, Ma ZY, Liu Y, Li S. Effect of solution temperature on aging behavior and properties of SiCp/Al–Cu–Mg composites. Mater Sci Eng A 2011;528:1504–11.

[40] Genevois C, Deschamps A, Denquin A, Doisneau-cottignies B. Quantitative investigation of precipitation and mechanical behaviour for AA2024 friction stir welds. Acta Mater 2005;53:2447–58.

[41] Aydin H, Bayram A, Ismail D. The effect of post-weld heat treatment on the mechanical properties of 2024-T4 friction stir-welded joints. Mater Des 2010;31:2568–77.

[42] Zhang Z, Xiao BL, Ma ZY. Effect of welding parameters on microstructure and mechanical properties of friction stir welded 2219Al-T6 joints. J Mater Sci 2012;47:4075–86.